

Maximum Entropy Reconstruction of the Interstellar Medium: I. Theory

John S. Arabadjis and Joel N. Bregman

University of Michigan

Ann Arbor, MI 48109-1090

jsa@astro.lsa.umich.edu

jbgregman@astro.lsa.umich.edu

ABSTRACT

We have developed a technique to map the three-dimensional structure of the local interstellar medium using a maximum entropy reconstruction technique. A set of column densities \mathbf{N} to stars of known distance can in principle be used to recover a three-dimensional density field \mathbf{n} , since the two quantities are related by simple geometry through the equation $\mathbf{N} = \mathbf{C} \cdot \mathbf{n}$, where \mathbf{C} is a matrix characterizing the stellar spatial distribution. In practice, however, there is an infinite number of solutions to this equation. We use a maximum entropy reconstruction algorithm to find the density field containing the least information which is consistent with the observations. The solution obtained with this technique is, in some sense, the model containing the minimum structure. We apply the algorithm to several simulated data sets to demonstrate its feasibility and success at recovering “real” density contrasts.

This technique can be applied to any set of column densities whose end points are specified. In a subsequent paper we shall describe the application of this method to a set of stellar color excesses to derive a map of the dust distribution, and to soft X-ray absorption columns to hot stars to derive a map of the *total* density of the interstellar medium.

Subject headings: ISM: general

1. Introduction

Given a set of projected density measurements of columns with known end points, one can, at least in principle, recover the three dimensional distribution of absorbing material.

One way to accomplish this deprojection is to simply draw isocolumn contours (Sfeir et al. 1999; Welsh et al. 1999). Here we propose an alternative technique – maximum entropy reconstruction (MER) – and apply a computer implementation of the algorithm to simulated data sets. We test its ability to recover structure in the interstellar medium (ISM) by varying several parameters and the functional form of the entropy. We then briefly sketch its application to a number of archived data sets, to be presented in a subsequent paper.

2. Maximum Entropy Technique

The column or projected density of absorbing material $N(\mathbf{x})$ along the line of sight between an observer and a star at position \mathbf{r}_\star is defined as

$$N(\mathbf{r}_\star) = \int_0^{r_\star} n(\mathbf{x}) dr \quad (1)$$

where $n(\mathbf{x})$ is the number density of absorbers at position \mathbf{x} , usually measured in cm^{-3} . It is $n(\mathbf{x})$, the map of the ISM, that we seek. Although the inversion of equation 1 is formally trivial, we know only N/r_\star , and so there is an infinite number of functions $n(\mathbf{x})$ which satisfy the observed $N(\mathbf{x}_\star)$. We therefore take a discrete approach, approximating the ISM as a coarse-binned density field.

Consider a set of data consisting of N_\star stars of known distance, to which accurate intervening column densities have been measured. We write the set of column densities to these N_\star stars as the vector $\mathbf{N} = (N_1, N_2, \dots, N_{N_\star})$. Let us divide the space occupied by these stars into N_c cells of size s . (In practice the cells need not be cubic – more generally we have s_x , s_y and s_z . For example, it is sometimes useful to set s_z to a large number to build a planar model of the ISM.) The model we seek consists of the set of number densities of these cells (\mathbf{n} , a vector of length N_c) which will reproduce the observed column densities. The observations form a constraint equation

$$\mathbf{N} = \mathbf{C} \cdot \mathbf{n}, \quad (2)$$

where \mathbf{C} is a matrix with N_c rows and N_\star columns describing the line-of-sight/cell intersections for each star.

For the moment, let us assume that the observer is located at the corner shared by 8 cells. (In the actual implementation of this algorithm we place the observer at the center of a cell, however, to enhance the numerical stability of several matrix inversions.) If s is small

enough, no two lines of sight will intersect the same cell, and there will be an infinite number of solutions to this equation. It is clear, however, that some solutions will be preferred over others. For example, let us imagine that our data set consists of only one stellar position and intervening column density. It is easy to imagine two different models – the minimum and maximum structure configurations (Figure 1) – which reproduce the observations. Figure 1a shows the material spread out evenly along the line of sight, whereas in Figure 1b the material inhabits only one cell. In the absence of any additional information both models reproduce the observations equally well. Information theory tells us that the former is to be preferred to the latter, however, since it makes the fewest assumptions about the underlying structure – i.e. it contains less information. Since our goal is to uncover structure in the ISM, the most conservative approach is to find the solution containing the minimum structure. Thus we seek a configuration which is a solution to equation 2 and which contains the minimum amount of information.

The quantity of information contained in a map is usually measured using the Shannon entropy (Shannon 1948; Kapur & Kesavan 1992). To construct the map with the fewest assumptions about the underlying structure, but consistent with a set of observations, we invoke Jaynes’ principle of maximum entropy (Jaynes 1957). The nomenclature “entropy” was adopted because the Shannon entropy was shown by Jaynes (1957) to be identical to the classical Boltzmann entropy.

In general, a map can be characterized by a distribution function $f = f(t, \mathbf{x}, \mathbf{v})$, where f is the mass per unit volume per velocity interval. The amount of information contained in the distribution is characterized by the Boltzmann H function,

$$H = \int f \log f \, d\mathbf{x} \, d\mathbf{v} \quad (3)$$

which is related to the thermodynamic entropy S through

$$H = -\frac{S}{kV} \quad (4)$$

Here V is the volume covered by the map, and k is Boltzmann’s constant.

The choice of grid resolution is fundamental to the character of the reconstructed map. We will choose a cell size s such that $v_{\text{ISM}} \cdot t_{\text{obs}} \ll s$, where v_{ISM} is the typical velocity of material in the ISM and t_{obs} is the timescale spanned by the observations. Thus we can ignore any time dependence in the phase space density, making it a function of cell position only. In addition, $v_{\text{ISM}} \ll c$ throughout the Galactic ISM, and so the absorptive properties

of the material in each cell are independent of the velocity of the material. Thus we replace $f(\mathbf{x}, \mathbf{v}, t)$ with the coarse-binned ρ_i . Scaling the entropy by the mean particle mass and Boltzmann’s constant we obtain

$$S = - \sum_{i=1}^{N_c} n_i \log n_i \quad (5)$$

where n_i is the number density of absorbers in cell i . The analogy between n_i and probability p_i of finding a particle in cell i leads immediately to the identification of equation 5 as the Shannon entropy. We shall, however, refer to this form as the “Boltzmann entropy” of the map, in keeping with past astrophysical applications of the maximum entropy principle.

In the present problem we are not restricted to using the Boltzmann entropy. Boltzmann’s H theorem was originally formulated to show that the thermodynamic entropy is the only non-decreasing function of the time-dependent distribution function for an ideal gas (Boltzmann 1896; Tolman 1938). In collisionless systems, however, there is an infinite number of H functions which exhibits this behavior (Tremaine, Hénon, & Lynden-Bell 1986). These are of the form

$$S = - \sum_{i=1}^{N_c} C_i(n_i) \quad (6)$$

where C is any convex function of the distribution function. Following Richstone & Tremaine (1988) we shall use the term “entropy” to refer to any function of this form, although, in the context of information, “uncertainty” might be a more appropriate term, as Kapur & Kesavan (1992) point out.

The ISM is an extremely complex physical system. Although it can be considered a “collisional” system in some sense, astrophysical processes such as radiative cooling, energy injection by supernovae, and self-regulating star formation render this characterization of its self-interaction too simplistic. Thus there are no compelling arguments based upon first principles which favor one form of the entropy over another. We shall instead turn to numerical experimentation and convenience to guide our choice of the entropy. We shall return to this topic in Section 3.1.

Regardless of the form of entropy we ultimately adopt, we seek the solution of equation 2 where S is a maximum, or, equivalently, we seek the map containing the minimum information. (Although there are many configurations wherein S is minimized, there is only one, for a given grid, where it is maximized.) This problem is readily solved using the method

of Lagrange multipliers (Jaynes 1957). For example, Richstone & Tremaine (1988) adapted this technique to solve the problem in a stellar dynamical context. We adopt this approach here, recasting it for the problem at hand.

The (generally nonlinear) variational equation we must solve is

$$\delta S - \delta \mathbf{N} \cdot \mathbf{L} = 0 \quad (7)$$

where the vector $\mathbf{L} = (L_1, L_2, \dots, L_{N_c})$ is the set of Lagrange multipliers to be determined later. In the limit of small variations we have

$$\nabla S - (\nabla \mathbf{N})^t \cdot \mathbf{L} = 0 \quad (8)$$

where the operator ∇ is defined as

$$\nabla = \hat{\mathbf{e}}_1 \frac{\partial}{\partial n_1} + \hat{\mathbf{e}}_2 \frac{\partial}{\partial n_2} + \dots + \hat{\mathbf{e}}_{N_c} \frac{\partial}{\partial n_{N_c}} \quad (9)$$

and $(\nabla \mathbf{N})^t$ is the transpose of $\nabla \mathbf{N}$. Since the column density is related to the number density through equation 2, $\nabla \mathbf{N} = \mathbf{C}$, and we have then

$$\nabla S - \mathbf{C}^t \cdot \mathbf{L} = 0 \quad (10)$$

To solve this equation we guess a solution \mathbf{n}_0 and iterate using the Newton-Raphson method. Expanding about the initial guess and keeping terms only to first order yields

$$\nabla S|_{\text{new}} = \nabla S|_{\mathbf{n}_0} + \nabla(\nabla S|_{\mathbf{n}_0}) \cdot \delta \mathbf{n} \quad (11)$$

Inserting equation 11 into equation 10, and solving for $\delta \mathbf{n}$ yields

$$\delta \mathbf{n} = (\diamond S|_{\mathbf{n}_0})^{-1} \cdot \mathbf{C}^t \cdot \mathbf{L} - (\diamond S|_{\mathbf{n}_0})^{-1} \cdot \nabla S|_{\mathbf{n}_0} \quad (12)$$

where $\diamond S \equiv \nabla(\nabla S)$. To make use of this equation we must first calculate the Lagrange multipliers. Dotting both sides with \mathbf{C} and solving for \mathbf{L} we obtain

$$\mathbf{L} = (\mathbf{C} \cdot \diamond S|_{\mathbf{n}_0}^{-1} \cdot \mathbf{C}^t)^{-1} \cdot \delta \mathbf{N} + (\mathbf{C} \cdot \diamond S|_{\mathbf{n}_0}^{-1} \cdot \mathbf{C}^t)^{-1} \cdot \mathbf{C} \cdot \diamond S|_{\mathbf{n}_0}^{-1} \cdot \nabla S|_{\mathbf{n}_0} \quad (13)$$

Here we have identified $\mathbf{C} \cdot \delta \mathbf{n}_0$ as $\delta \mathbf{N}$, the difference between the observations and the model column densities corresponding to the guessed solution \mathbf{n}_0 . Equation 12 is applied iteratively, with the Lagrange multipliers calculated anew at each step using equation 13, until a satisfactory solution is obtained. The computational expense is dominated by the inversion of $\diamond S$, an $N_c \times N_c$ matrix.

The density of material in each cell is physically (though not mathematically) restricted to non-negative values. In order to impose this condition upon our solution we require that each component of $\delta \mathbf{n}$, as calculated in the code by equation 12, be no greater in magnitude than the current value of density in that cell. This guarantees that each cell has a non-negative density at every step in the iterative reconstruction and in the final maximum entropy solution.

3. Simulated Data Sets

When we apply the MER algorithm to a real data set, we will not know whether the resultant map is close to the actual ISM structure. (We can be sure that the reconstructed map is very different from the true structure if the iteration scheme fails to converge, however.) To ascertain how well the algorithm reconstructs underlying distribution of absorbing matter we must test its performance upon simulated data sets. We postulate a 3D density structure $n(\mathbf{x})$ for the ISM and a stellar spatial distribution, and calculate $N(\mathbf{x}_*)$ for each star using equation 1. We then apply the MER algorithm to the faked data set $\mathbf{N}(\mathbf{x}_*)$ and compare the maximum entropy configuration with the simulated density structure.

There are three aspects of the scheme which need to be explored using these simulated data. These are (1) the form of the entropy used in the maximization routine, (2) the size of the spatial cells used, for a given sampling density, and (3) the sampling density of the stars in the data set, compared with the scale length of the smallest structures in the ISM.

3.1. Functional Form of the Entropy

A strict interpretation of information theory dictates that the entropy we should maximize is the Shannon entropy (i.e. the classical Boltzmann entropy), in the form given by equation 5. However, in the spirit of experimentation, we also ran tests for three other forms of the entropy as well. Two of these are “true” entropies in the the sense of Tremaine, Hénon, & Lynden-Bell (1986), following the form of equation 6. They are

$$S = - \sum_{i=1}^{N_c} n_i^2 \quad (14)$$

and

$$S = - \sum_{i=1}^{N_c} e^{n_i} \quad (15)$$

The former, because it is a simple quadratic, should converge in only one iteration in the Newton-Raphson scheme. The fourth function we tried was

$$S = \sum_{i=1}^{N_c} n_i e^{-n_i} \quad (16)$$

This function is not of the form given by equation 6, and so we refer to it as a “pseudo-entropy”. Although it is not of the form discussed by Tolman (1938) and Tremaine, Hénon, & Lynden-Bell (1986), like these other forms it possesses a single global maximum – a property which, as it turns out, is probably sufficient to guarantee its utility. The four entropy types are compared in Figure 2.

The simulated density field used for this experiment is shown in Figure 3. It consists of an ambient medium with a density of $\sim 0.1 \text{ cm}^{-3}$, with two structures superimposed upon it. One is a wall of material with a gaussian amplitude $\sim 150 \text{ cm}^{-3}$; the other is a small cloud with gaussian amplitude $\sim 70 \text{ cm}^{-3}$. The entire map has dimensions of $1017.5 \text{ pc} \times 632.5 \text{ pc}$.

Throughout this density field we distribute 458 stars in a random fashion (but with a minimum separation) and use the calculated columns to try to reconstruct the field. MER maps for the four entropy types given by equations 5, 14, 15, and 16 are shown in Figure 4. Each reconstruction uses a cell size of $27.5 \text{ pc} \times 27.5 \text{ pc}$, for a total grid size of 37×23 . Only 806 of the 851 cells are active in the reconstruction, however, because many edge cells are not pierced by a stellar line of sight. (These cells, shown in dark gray, are obvious toward the edges because they contain no stars.) We have set a column match tolerance of 10^{-4} for convergence termination, although in practice this will be set by the column measurement accuracy. (It should be noted that the cell size was optimized for this example.) Table 1 lists the mean column error, rms column error, the mean density error, and the rms density error, for each of the reconstructions. Quantities with the *mer* subscript obviously refer to properties of the reconstruction. Column densities with no subscript represent the input data, while number densities with no subscript represent the density of the “actual” configuration at the cell center.

Two conclusions can be drawn from this experiment. The first is that MER is an effective way to recover real density contrasts without introducing significant spurious structure. Both structures are clearly reproduced by the algorithm with the appropriate amplitudes. And in no case do we find extraneous structure on scales larger than a pixel.

The second observation is that the MER algorithm is quite insensitive to the form of the entropy used. The reconstructions created using the four different entropy types are nearly identical; in fact, one would be hard-pressed to distinguish one from another without referring to Table 1. Even the pixel-sized variations occur in the same location, suggesting that the “noise” in each reconstructed map is due to the peculiarities of the stellar distribution with respect to the cell grid, rather than tied to a specific form of the entropy. We therefore conclude that it is best to use the quadratic entropy, to save on computational expense. If we normalize the time to calculate the entropy and its derivatives to the that of the quadratic form, we have $t_{\text{Boltz}} = 1.3$, $t_{\text{expo}} = 1.5$, and $t_{\text{pseudo}} = 2.0$.

In practice, program run-times are actually *much* shorter using the quadratic entropy because the MER algorithm usually converges in one or two iterations, compared with four to seven for the other entropy types. These run-time savings are greatest when the grid contains a large number of cells (and by extension a large number of stars, since they scale linearly in optimized configurations). In the 458-star simulation, a single iteration of the code running on a 450 MHz Pentium II processor took 52 s when using a grid of 684 cells, and 1230 s with a 2285-cell grid (see Section 3.2). So while using the quadratic entropy may only save a few minutes for a small number of stars, the difference can be several hours for a large data set.

3.2. Cell size

We next sought to understand the importance of cell size for a given stellar sampling density. The number density of the ISM should really be calculated differentially from the column data through equation 1; the MER algorithm, however, uses a differencing scheme. Since the number density of absorbers in a particular cell is constant across the cell in the reconstructed map, we expect there to be numerical instabilities when the cell size is comparable to or larger than the size scale of structures in the underlying ISM. If the cell is so large that it contains two stars, and a non-negligible density gradient, there may actually be no solution to the constraint equation, regardless of any entropy considerations.

We examined the effect of cell size modulation on the reconstructed map, for a fairly dense simulated stellar distribution. For this set of experiments we use the simulated density

map shown in Figure 5. It contains three clouds of various size scale and maximum density. From largest to smallest, the gaussian amplitudes are $\sim 100, 40,$ and 35 cm^{-3} . The entire map has dimensions of $1012.5 \text{ pc} \times 607.5 \text{ pc}$, with 666 stars distributed throughout. We varied the cell size from 27.5 pc on a side, down to 12.5 pc, in increments of -2.5 pc . These MER maps are shown in Figure 6.

Table 2 gives the error statistics for each reconstruction. We omit the 27.5 pc cell MER map because the reconstruction failed – the algorithm was terminated after one iteration because the solution was divergent. The reason for this is that several cells contain two stars and a sufficiently steep density gradient, resulting in zero solutions of the constraint equation. Each of the reconstructions shown in Figure 6 fit the data reasonably well (the column tolerance was set to 10^{-3}). As the cell size decreases, however, the solution begins to show radial striations as more and more cells are intersected by only one or two stellar lines of sight. In the limiting case of infinitesimal cells, every active cell in the grid is pierced only once; in essence, each individual line of sight reduces to the configuration illustrated in Figure 1. Thus material is smeared evenly along each absorption path, and the $N_\star \times N_c$ optimization problem reduces to N_\star separate $\alpha_k N_c$ problems ($\sum_{k=1}^{N_\star} \alpha_k = 1$). Since no cell is intersected by more than one line of sight, these paths no longer “communicate” with each other, and their individual entropy contributions decouple during the optimization.

For this particular case the solution is optimized (in the sense of matching the “true” 3D density) for a cell/star ratio of about 7/4. However, barring peculiarities in stellar position within each cell, $\langle N_{mer} - N \rangle \rightarrow 0$ as the cell size is reduced. It would be identically zero once each cell is pierced by only one stellar line of sight, although the number density errors would grow as structure is washed out along the line of sight.

3.3. Sampling density

Finally we examined the ability of the algorithm to detect ISM structures for a limited stellar sampling density. Again we use the simulated ISM of Figure 5. We ran twelve MER reconstructions for N_\star from 13 to 342, with optimized cell numbers from 22 to 342 (Figure 7; Table 3). Using a column tolerance of 10^{-4} , the cell size was varied in increments of 5 pc to find the best reconstruction. Again, dark gray cells toward the edges which contain no stars are disregarded in the MER.

The reconstruction using 13 stars can detect only the largest of the three clouds. The map is, however, quite good, considering that it gets the amplitude right, and matches the columns to within 0.003%. The reconstruction using 34 stars probably resolves the small

cloud closest to the sun. The 48-star map may actually resolve both small clouds, although it is not a robust detection. Although the column fit is nearly perfect, the map shows an unfortunate feature common to low-density sampled maps – the MER algorithm awards the pixel containing the sun an excess of material, at the expense of the 8 pixels which surround it. Thus if the goal of the reconstruction is to study the *very* local ISM, one cannot trust a high density contrast in only the central (solar) bin. By the time we get to 120 and 177 stars, both small clouds are clearly detected, as is the low-density bridge between the two largest clouds. Clearly, the sample of stars must be sufficiently dense such that the ISM structures to be detected are at least as large as the mean spacing between stars.

4. Summary and applications

Maximum entropy reconstruction is a powerful technique for recovering the structure of the ISM from column density data sets. By modulating the cell size, one can find a solution which recovers the underlying structure in the ISM. The lower limit to the size scale of detected structures is set by the stellar sampling density. The reconstruction algorithm is insensitive to the particular form of the entropy employed, so it is most prudent to use computationally simple and rapidly converging forms such as the quadratic entropy (equation 14).

The next step is to apply this technique to existing astronomical data sets. Different components of the ISM can be traced by absorption and emission measurements made at different wavelengths. Using a variety of absorptive and emissive tracers, we should be able to map regions of varying ionization and molecular state and elemental composition, and compare their spatial distributions.

We are currently working to map the distribution of dust in the ISM using column densities derived from stellar color excess measurements. In addition, we are using archived *ROSAT* observations of hot stars to determine X-ray absorption columns. Since the soft X-ray cross section is insensitive to the molecular and (modest) ionization state of the absorber (Arabadjis & Bregman 1999), reconstructing the density field using X-ray columns will map the *total* density of material the local ISM. Additionally, by exploiting the spectral resolution of instruments aboard XMM-Newton and Chandra, one may be able to separate this material by ionization state. For example, $\Delta E/E \sim 50$ for the non-dispersive ACIS detector aboard Chandra, resulting in a spectral resolution of about 10 eV at the prominent absorption edge of oxygen at 0.5 keV. Since the neutral and first three ionization states of oxygen are separated by about 20 eV each (the potentials are 13.6, 35.1, and 54.9 eV), it may be possible to distill the oxygen distribution into its dominant ionization states.

Several ISM tracers also contain velocity information. Optical absorption lines in stellar spectra, originating from the ISM, provide a measure of the distribution of metals not bound up in dust grains, and maps constructed from their columns may provide insight into the gas phase chemistry of ISM. Additionally, the velocity structure of a resolved absorption line can be used in conjunction with a rotation curve and a second application of the maximum entropy principle to further constrain the distribution of material along the line of sight. Similarly, velocity-resolved 21 cm emission maps can be used to construct a distribution of neutral hydrogen along each line of sight.

The applicability of this technique to absorption measurements at almost any wavelength comes at a particularly fortuitous time. Most astronomical satellite programs support an on-line archive containing their public domain observations, many of which can be mined for projected density measurements. With the number number of of these archives growing on an almost daily basis, this technique should find wide application in the near future.

The authors would like to acknowledge support from NASA grant NAG5-3247. JSA would like to thank Doug Richstone for useful discussions.

REFERENCES

- Arabadjis, J.S., & Bregman, J.N. 1999, ApJ, 510, 806
- Boltzmann, L. 1896, Vorlesungen über Gastheorie, I. Theile (Leipzig: J.A. Barth)
- Jaynes, E.T. 1957, Physical Reviews, 106, 620
- Kapur, J.N., & Kesavan, H.K. 1992, Entropy Optimization Principles with Applications (London: Academic Press)
- Richstone, D.O., & Tremaine, S. 1988, ApJ, 327, 82
- Sfeir, D.M., Lallement, R., Crifo, F. & Welsh, B.Y. 1999, A&A, 346, 785
- Shannon, C.E. 1948, Bell System Tech. J., 27, 379 & 623.
- Tolman, R. C. 1938, The Principles of Statistical Mechanics (Oxford: Clarendon Press)
- Tremaine, S., Hénon, M., & Lynden-Bell, D. 1986, MNRAS, 219, 285
- Welsh, B.Y., Sfeir, D.M., Sirk, M.M., & Lallement, R. 1999, A&A, 352, 308

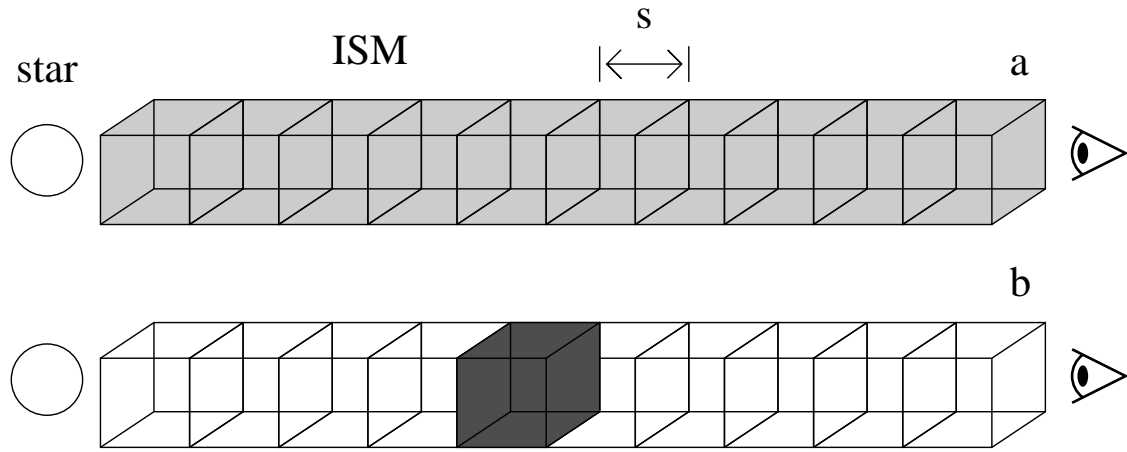


Fig. 1.— Two discrete-bin ISM models which result in the same intervening column density toward a star.

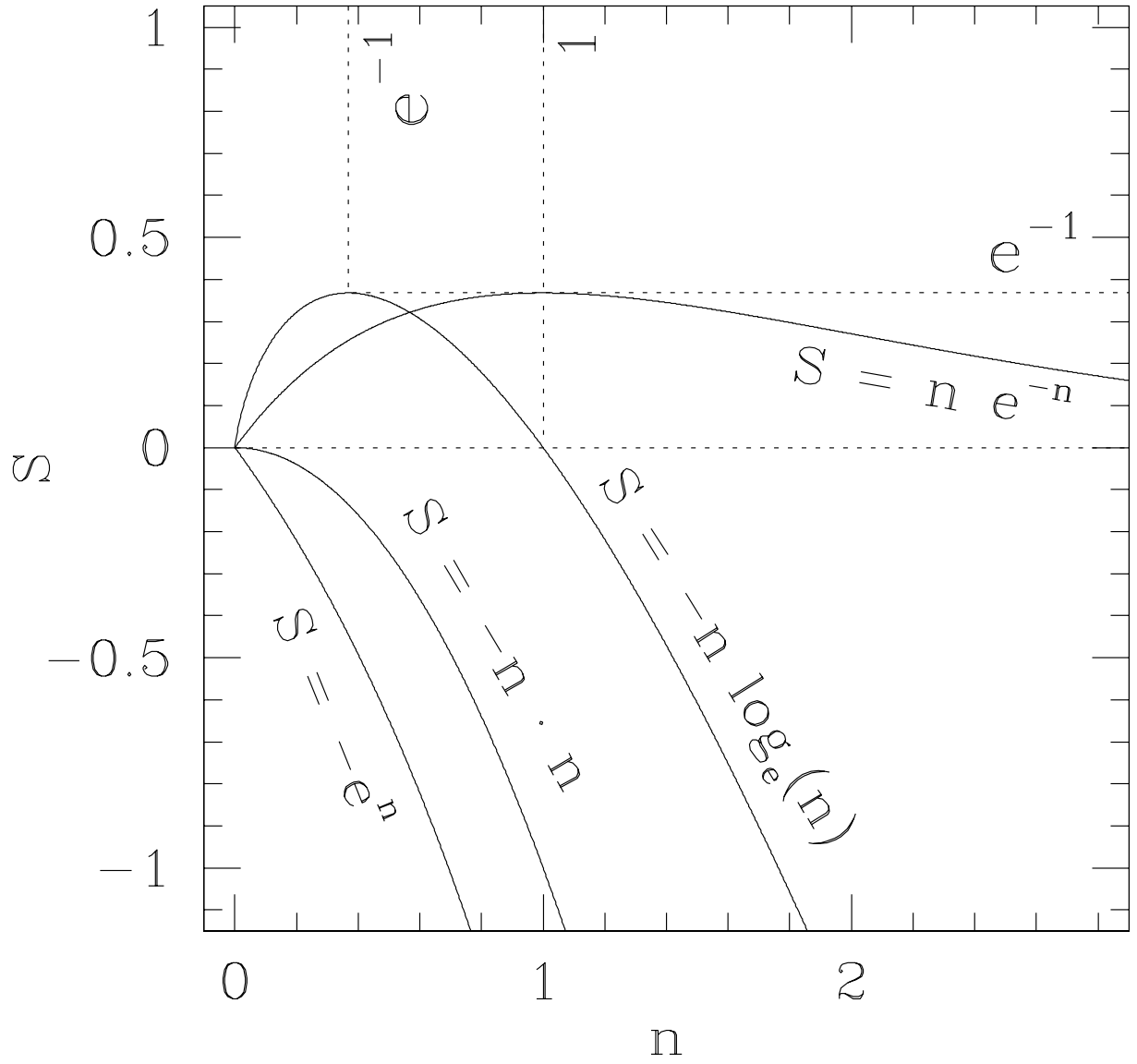


Fig. 2.— The four entropy forms examined in this study. Note the concavity inflection of the pseudo-entropy $S = n e^{-n}$ at $n = 2$.

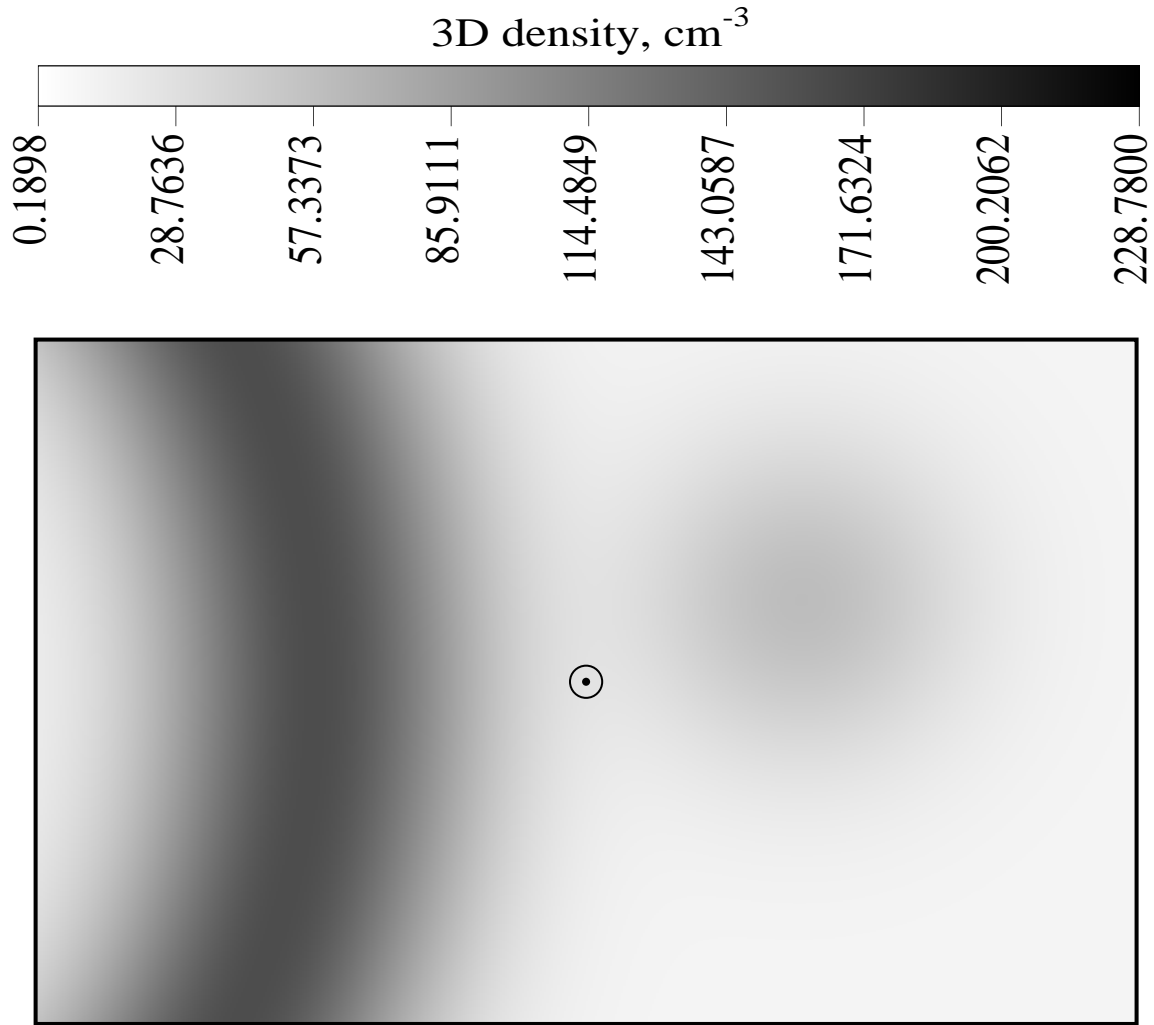


Fig. 3.— Simulated density map used to gauge the effect of changing the form of the entropy used in the reconstruction. The filled black dots represent the location of the stars whose intervening columns are used in each map reconstruction. The observer location is shown by the sun symbol at the map center.

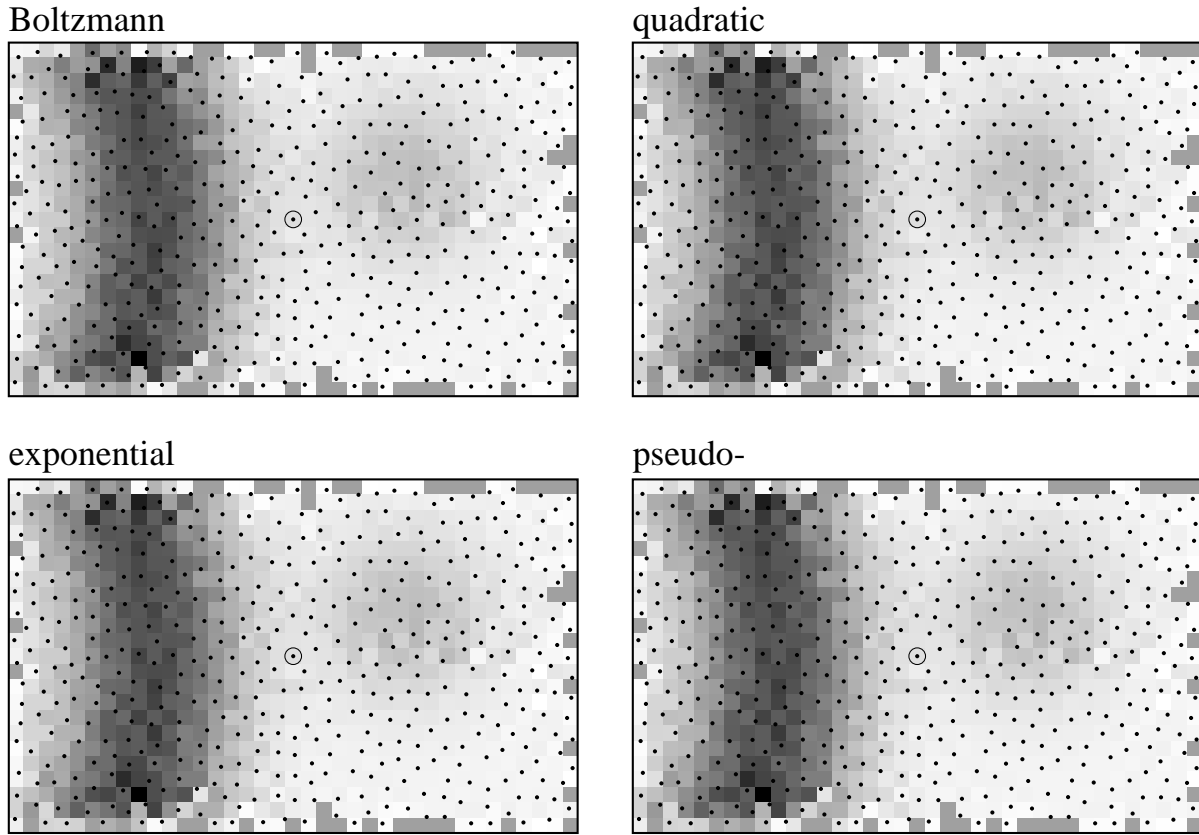


Fig. 4.— Maximum entropy reconstructions of the density field shown in Figure 3 using four different entropy functions. The maps are nearly indistinguishable.

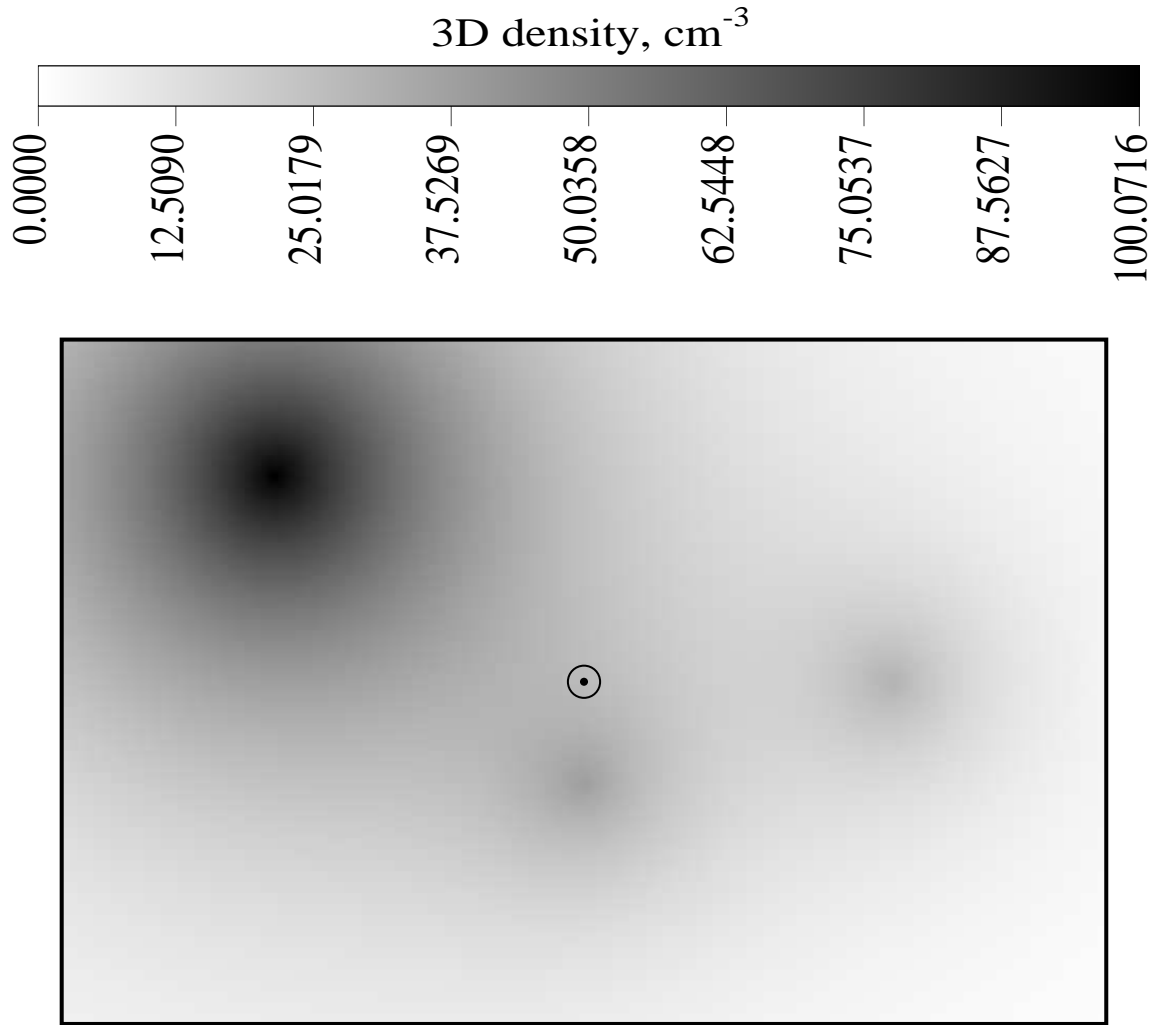


Fig. 5.— Simulated density field used to gauge the effect of modulating the cell size for a given stellar sampling density (Figure 6) and for modulating the stellar sampling density using an appropriate cell size (Figure 7).

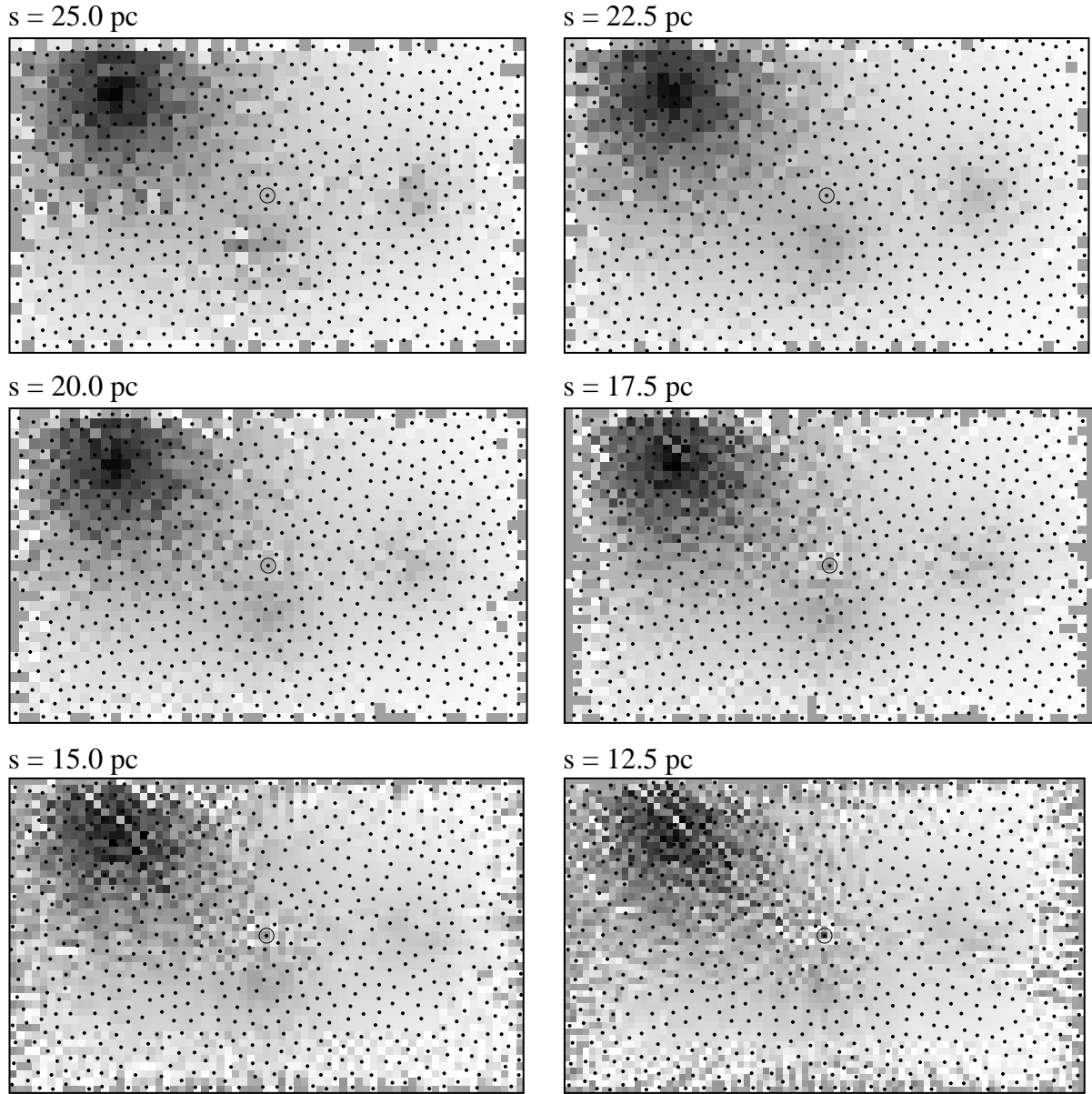


Fig. 6.— Maximum entropy reconstructions of the density field shown in Figure 5 using a range of cell sizes.

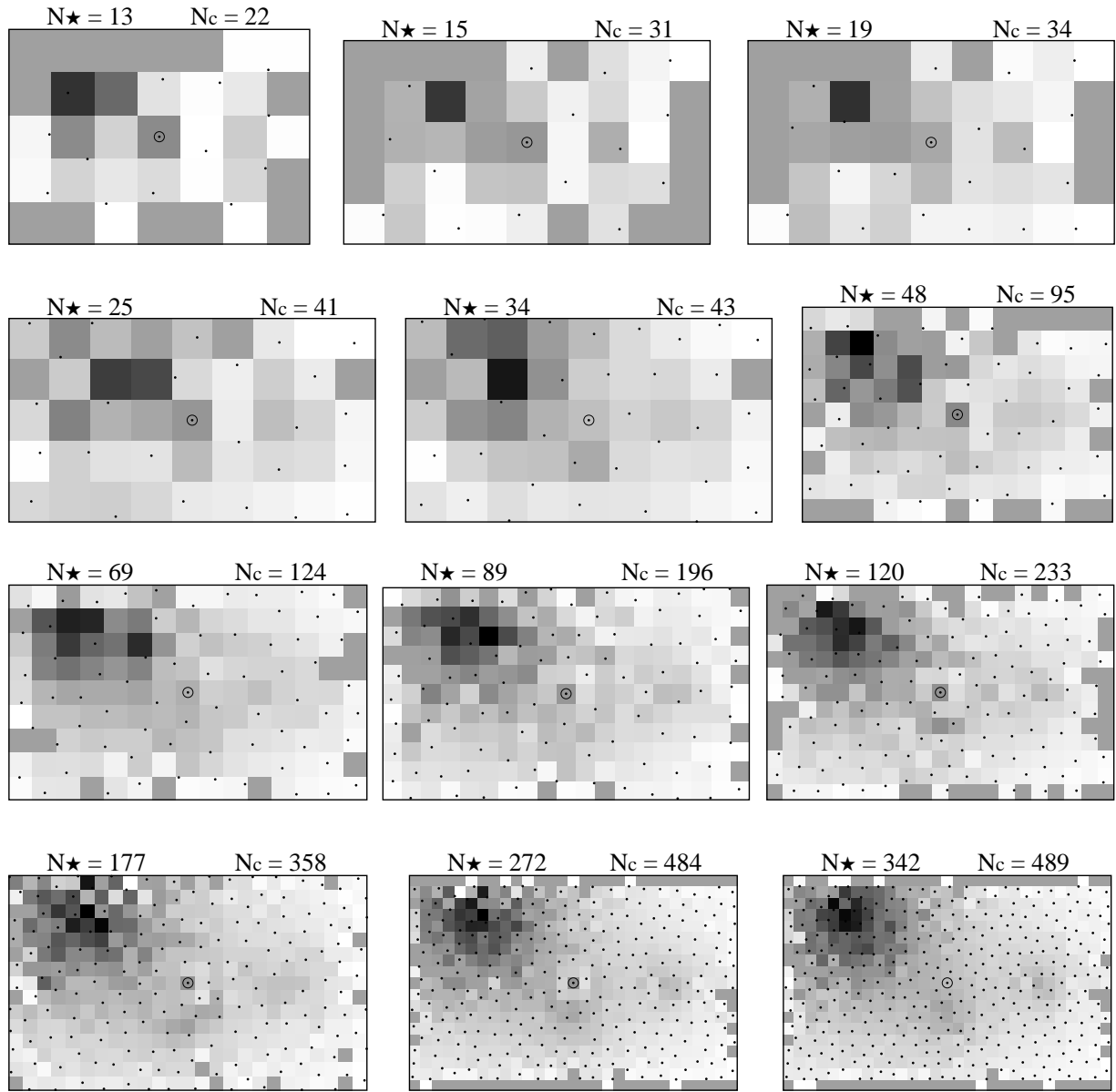


Fig. 7.— Maximum entropy reconstructions of the density field shown in Figure 5 using a range of stellar sampling densities and roughly optimized for cell size.

Table 1. Maximum entropy reconstructions of the simulated data set shown in Figure 3, for four different entropy functions. Relative errors are shown in parentheses.

entropy type	functional form	$\langle N_{mer} - N \rangle$ (cm^{-2})	$\sqrt{\langle (N_{mer} - N)^2 \rangle}$ (cm^{-2})	$\langle n_{mer} - n \rangle$ (cm^{-3})	$\sqrt{\langle (n_{mer} - n)^2 \rangle}$ (cm^{-3})
Boltzmann	$S = -\sum n_i \log n_i$	7.68×10^{16} (0.000 003)	6.41×10^{17} (0.000 017)	-2.90 (-0.0697)	16.4 (0.277)
quadratic	$S = -\sum n_i^2$	2.56×10^{17} (0.000 003)	1.53×10^{18} (0.003 028)	-2.90 (-0.0697)	16.4 (0.277)
exponential	$S = -\sum e^{n_i}$	7.34×10^{17} (0.000 025)	1.74×10^{18} (0.000 049)	-2.90 (-0.0697)	16.4 (0.277)
pseudo-	$S = \sum n_i e^{-n_i}$	2.84×10^{17} (0.000 003)	1.96×10^{18} (0.003 031)	-2.82 (-0.0657)	16.2 (0.265)

Table 2. Maximum (quadratic) entropy reconstructions of the simulated data set shown in Figure 5, for variable cell size s . Relative errors are shown in parentheses.

s (pc)	N_c	$\langle N_{mer} - N \rangle$ (cm^{-2})	$\sqrt{\langle (N_{mer} - N)^2 \rangle}$ (cm^{-2})	$\langle n_{mer} - n \rangle$ (cm^{-3})	$\sqrt{\langle (n_{mer} - n)^2 \rangle}$ (cm^{-3})
25.0	979	-1.22×10^{19} (-0.000 716)	3.42×10^{19} (0.001 85)	-0.917 (-0.0535)	6.41 (0.259)
22.5	1178	-1.61×10^{17} (0.000 011)	9.96×10^{17} (0.000 040)	-0.865 (-0.0505)	5.43 (0.218)
20.0	1484	-3.35×10^{17} (0.000 014)	7.05×10^{20} (0.000 028)	-1.23 (-0.0672)	6.41 (0.255)
17.5	1888	8.09×10^{16} (0.000 006)	1.39×10^{18} (0.000 040)	-1.39 (-0.0686)	7.03 (0.264)
15.0	2512	1.79×10^{17} (0.000 005)	1.07×10^{18} (0.000 037)	-1.65 (-0.0807)	7.75 (0.294)
12.5	3477	1.36×10^{19} (0.000 959)	3.83×10^{19} (0.003 37)	-1.97 (-0.0919)	8.58 (0.325)

Table 3. Maximum (quadratic) entropy reconstructions of the simulated data set shown in Figure 5, for variable N_\star and optimized cell size. Relative errors are shown in parentheses.

N_\star	s (pc)	N_c	$\langle N_{mer} - N \rangle$ (cm^{-2})	$\sqrt{\langle (N_{mer} - N)^2 \rangle}$ (cm^{-2})	$\langle n_{mer} - n \rangle$ (cm^{-3})	$\sqrt{\langle (n_{mer} - n)^2 \rangle}$ (cm^{-3})
13	190	22	7.692×10^{17} (0.000 031)	2.773×10^{18} (0.000 113)	-2.387 (-0.2897)	10.06 (0.7598)
15	140	31	0.0000×10^{17} (0.000 000)	0.0000×10^{18} (0.000 000)	-2.730 (-0.1166)	9.151 (0.6934)
19	140	34	0.0000×10^{17} (0.000 000)	0.0000×10^{18} (0.000 000)	-1.387 (-0.1039)	7.258 (0.5876)
25	125	41	0.0000×10^{17} (0.000 000)	0.0000×10^{18} (0.000 000)	-2.540 (-0.1003)	12.80 (0.4770)
34	120	43	0.0000×10^{17} (0.000 000)	0.0000×10^{18} (0.000 000)	-0.5711 (-0.01688)	8.198 (0.2676)
48	80	95	0.0000×10^{17} (0.000 000)	0.0000×10^{18} (0.000 000)	-2.826 (-0.1266)	10.88 (0.3787)
69	70	124	0.0000×10^{17} (0.000 000)	0.0000×10^{18} (0.000 000)	-2.687 (-0.1169)	10.74 (0.3426)
89	55	196	0.0000×10^{17} (0.000 000)	0.0000×10^{18} (0.000 000)	-2.544 (-1381)	9.424 (0.3753)
120	50	233	0.05×10^{17} (0.000 001)	0.0258×10^{18} (0.000 003)	-1.980 (-0.09216)	8.327 (0.3169)
177	40	358	0.011×10^{17} (0.000 000)	0.0106×10^{18} (0.000 001)	-1.692 (-0.08350)	8.556 (0.2961)

Table 3—Continued

N_\star	s (pc)	N_c	$\langle N_{mer} - N \rangle$ (cm^{-2})	$\sqrt{\langle (N_{mer} - N)^2 \rangle}$ (cm^{-2})	$\langle n_{mer} - n \rangle$ (cm^{-3})	$\sqrt{\langle (n_{mer} - n)^2 \rangle}$ (cm^{-3})
272	35	484	2.217×10^{17} (0.000 007)	1.907×10^{18} (0.000 029)	-1.274 (-0.05995)	7.527 (0.2609)
342	35	489	-1.447×10^{17} (-0.000 041)	18.60×10^{18} (0.000 385)	-1.178 (-0.0597)	6.801 (0.2549)